Materials Research Bulletin 105 (2018) 121–125

Contents lists available at ScienceDirect

Materials Research Bulletin

journal homepage: www.elsevier.com/locate/matresbu

Structural, morphological, optical and magnetic properties of $Ag_{3(2+x)}In_xNb_{4-x}O_{11+\delta}$ ($0.25 \leq x \leq 1.0$) nanoparticles synthesized by sol–gel method

S. Ramesh[a,b,*], Jerald V. Ramaclus[c], B.B. Das[d], Edgar Mosquera[a,e]

[a] Laboratorio de Materiales Funcionales a Nanoescala, Departamento de Ciencia de los Materiales, Universidad de Chile, Beauchef 851, Santiago, Chile
[b] Saveetha School of Engineering, Saveetha University, Chennai, 602105, India
[c] Department of Physics, St. Joseph's College, Tiruchirappalli, Tamil Nadu, 620002, India
[d] Department of Chemistry, Pondicherry University, Pondicherry, 605014, India
[e] Departamento de Física, Universidad del Valle, A.A. 25360, Cali, Colombia

ARTICLE INFO

Keywords:
Sol-gel preparation
Nanoparticles
Semiconductors
Magnetic materials

ABSTRACT

Herein, we report the structure, morphology, optical and magnetic properties of novel $Ag_{3\ (2+x)}\ In_xNb_{4-x}O_{11+\delta}$ ($0.25 \leq \times \leq 1.0$; A1–A4) nanoparticles prepared by sol-gel technique. The samples were studied using X-ray diffraction, electron microscopy, diffuse reflectance spectroscopy, vibrating sample magnetometer, and electron spin resonance. X-ray diffraction studies confirm the formation of monoclinic lattice type with P2/m space group. Purity and homogeneity of the samples were confirmed by X-ray mapping. The semiconductor nature of the samples was identified by optical absorption spectra which indicate an inter-band transition from the oxygen 2p to niobium 4d electronic states. The magnetization plots reveal the room temperature ferromagnetic behavior of the samples.

1. Introduction

Silver-niobium based compounds have been widely investigated multifunctional materials for the promising applications as ferroelectrics, piezoelectrics, thermoelectrics, dye-sensitized solar cells, catalysis, optical devices and degradation of organic pollutants [1–4]. The properties of niobium oxide can be tailored according to the desired application simply by doping of metal and non-metals, in particular, the doping of noble metals like silver into niobium oxide is expected to increase the carrier mobility. This relatively higher delocalization of 3d orbitals may share in hybridization of the energy band structure which inturn increases the catalytic activity [5]. Recently, several series of niobium incorporating multifunctional metal oxides with the general formula of $A_{n+1}B_nO_{3n+1}$, $AA'_{n-1}Nb_nO_{3n+1}$ (A = K, Rb, Cs, Cu; A' = Bi, Ba, Pr, la), $Ag_{3(2+x)}Pr_x\ Nb_{4-x}O_{11+\delta}$, $A_nNb_{3n+1}O_{8n+3}$ (A = Ca, Na, K, Cu, Ag) are found to exhibit different properties like ferroelectrics, photocatalysis and phase transitions [6–9]. On the other hand, Indium oxide (In_2O_3), is a commonly used compound in the applications of transistors, sensors [10], solar cells [11,12], photocatalysis [13], field emission devices and window heaters [14]. It is generally used as a dopant to generate charge carriers of suffucient quantity to increase the electrical conductance of solar cells [15–17]. Therefore the combination of silver, indium and niobium oxides can result in interesting multifuctional properties which have not yet been investigated. One of the possibility when indium is integrated into silver-niobium system is, to improve the charge carriers which may help to further increase electrical conductivity of the system [16]. Thus, Ag_2O, Nb_2O_5, and In_2O_3 are excellent candidates for multifunctional nanomaterials for meeting the requirements of advanced science applications in the future. In our previous work, $Ag_{3(2+x)}Pr_xNb_{4-x}O_{11+\delta}$ was identified as stable multiferroic material. Therefore, in this article, we report a sol-gel synthesis route for obtaining $Ag_{3(2+x)}In_xNb_{4-x}O_{11+\delta}$ ($0.25 \leq \times \leq 1.0$; A1-A4) nanoparticles for the first time and study their optical absorbance, electrical and magnetic properties, at room temperature.

2. Experimental

2.1. Synthesis of $Ag_{3(2+x)}In_xNb_{4-x}O_{11+\delta}$ ($0.25 \leq \times \leq 1.0$) nanoparticles

Nanocrystalline $Ag_{3(2+x)}In_xNb_{4-x}O_{11+\delta}$ ($0.25 \leq \times \leq 1.0$) samples are prepared using sol-gel technique. Reagents are used without purification. Niobium citrate was synthesized using the required quantity of niobium oxide as described in our previous paper [5]. Niobium

* Corresponding author at: Laboratorio de Materiales Funcionales a Nanoescala, Departamento de Ciencia de los Materiales, Universidad de Chile, Beauchef 851, Santiago, Chile.
E-mail address: rsivasamy@ing.uchile.cl (R. S.).

https://doi.org/10.1016/j.materresbull.2018.04.049
Received 30 May 2017; Received in revised form 9 April 2018; Accepted 27 April 2018
Available online 30 April 2018
0025-5408/

citrate, indium and silver nitrate solutions were mixed and stirred for 1 h then 1.5 M citric acid solution of 30 ml were added into the resulting the solution mixture. The pH of the solution is maintained at 6 using liquid ammonia. The above solution is stirred continuously at 333 K till it converts a clear gel. The gel was broken at 473 K for 1 h. Finally, sintered for 4 h at 1123 K to achieve a well homogeneous condensed powder. The systematic preparation of the nanoparticles and the calculated amount of precursors aregiven in the supplementary information.

2.2. Characterization

The room temperature X-ray diffraction (PXRD) patterns were recorded by X'Pert PANalytical X-ray diffractometer in Bragg-Brentano configuration with monochromatic Cu Kα radiation (Cu Ka 1, 2 (λ ~ 1.54060, 1.54443 A), as a source and 40 kV/30 mA power. A scanning electron microscope (SEM) Hitchi-S3400 was used to investigate the morphology of the samples. The SUPER DRYER II was used to identify the element compositions and its distribution. The thermal analysis was done using TA Q600 SDT in the temperature range of 50–1000 °C at 10 °C/s under the N_2 atmosphere. The optical absorption spectra by a Varian Cary 5000 UV–VIS spectrometer. Magnetic properties by a LAKESHORE VSM 7404 vibrating sample magnetometer (VSM). The electron spin resonance (ESR) experiments at 77 and 300 K were performed with a JEOL JES-TE 100 ESR spectrometer at 100 kHz field modulation and magnetic field calibration was made with respect to the resonance line of DPPH (g_{DPPH} = 2.0035) as a field marker [18].

3. Results and discussion

3.1. X-ray diffraction studies

Powder X-ray diffraction patterns of $Ag_{3(2+x)}In_xNb_{4-x}O_{11+\delta}$ ($0.25 \leq \times \leq 1.0$; A1–A4) nanoparticles with corresponding (*hkl*) planes are shown in Fig. 1. In PXRD patterns, all the principal peaks are at the same diffraction angle which confirms the single-phase polycrystalline nature of the samples. The structural analysis was obtained using FullProf package. The least-squares procedure was used to index the diffraction peaks. The XRD result of A1–A4 shows comparable lattice parameters of the monoclinic lattice type with P2/m space group. To study the effect of In ions concentration, we pay attention to the XRD patterns the three peaks at 38°, 44° and 64° increases with increasing concentration of In ions. Similarly, the peak at 46° reduces from A1-A4, indicates the reducing the concentration of Nb ions in the samples. The average crystallite sizes were calculated from the XRD patterns by the Debye-Scherrer and Williamson-Hall methods [19,20]. The methods (1) and (2) are shown below

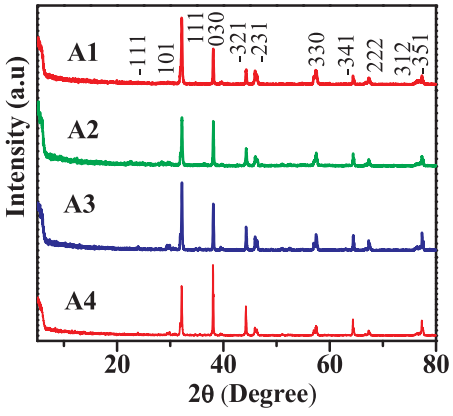

Fig. 1. XRD patterns of $Ag_{3(2+x)}In_xNb_{4-x}O_{11+\delta}$ ($0.25 \leq \times \leq 1.0$; A1–A4) nanoparticle.

Table 1
Lattice parameters, crystallite sizes, magnetic properties of $Ag_{3(2+x)}In_xNb_{4-x}O_{11+\delta}$ ($0.25 \leq \times \leq 1.0$; A1–A4) nanoparticles.

Sample code		A1	A2	A3	A4
Lattice type		Mono	Mono	Mono	Mono
a (Å)		7.5074	7.5063	7.5050	7.5124
b (Å)		7.0800	7.0764	7.0776	7.0864
c (Å)		5.0018	4.9984	5.0041	4.9947
β		119.09	119.11	119.14	119.00
Unit cell volume		232.30	231.96	232.15	232.54
Space group		P2/m	P2/m	P2/m	P2/m
Crystallite Size (nm)	Scherer	23.0	24.3	21.3	19.9
	WH Plot	26.7	23.2	25.1	26.4
χ x10⁻5 (emu/gG)		1.08	2.17	21.35	12.01
H_{ci} (G)		175.92	222.20	148.42	241.15
M_s (emu/g)		0.027	0.021	0.037	0.046
$M_r \times 10^{-3}$(emu/g),		0.60	0.73	1.09	1.69
g matrix	300 K	2.0368	2.0225	2.0099	2.0001
	77 K	2.0310	2.0302	2.0012	2.0301

Mono = Monoclinic.

$$D = 0.89\lambda/\beta_1/2\cos\theta_{hkl} \quad (1)$$

$$\beta\cos\theta = K\lambda/D + 2\varepsilon\sin\theta \quad (2)$$

Where D- crystallite size, λ- wavelength of Cu Kα radiation, β- half-width of the diffraction peak, θ- Bragg angle, K- Scherer constant, and ε-lattice strain. It is realized that the average crystallite sizes are increasing with increasing content of the In^{3+} ion. The increasing crystallite size is due to the change in higher ionic radius of In^{3+} (94 pm) ions with the smaller Nb^{4+} (82 pm) ions. The lattice parameters and crystallite sizes are reported in Table 1.

3.2. Morphology analysis

Morphological examinations were executed by SEM, and quantitative analysis by the EDS profile of arbitrarily selected particles of the samples (A1–A4) are shown in Fig. 2. The SEM images of the samples show the formation of the regular spherical nanoparticle. The noticeable particle size by SEM differs from the calculated XRD due to the fact, the XRD crystallite sizes are the mean of the several crystallographic orientations whereas the particle size by SEM is maybe shaped by several crystallites. As well, the EDS patterns of randomly selected particle of the sample A1-A4 are presented in Fig. 2. The EDS patterns confirm the presence of Ag, In, Nb and O ions without any impurities. To ensure the homogeneity and dispersion of the elements, the element mapping was employed for the randomly selected areas of samples (A1–A4) along with point selection of A4. The elemental map shows the concentrations of Ag, In, Nb and O ions which suggest that integrated all the elements are present and they are distributed uniformly (Supplementary information) which further confirms the purity of the sample. EDS profile with elemental X-ray maps reveal that the sol-gel method is extremely effective to prepare the multifunctional nanostructures.

3.3. Thermal analysis

Thermal stability of the materials is one of the key parameters for determining their commercial applications. The DTA curves of the samples are shown in Fig. 3. In high temperature, only the sample A4 show a broad exothermic peak at 538 °C which implies that oxidation process may remove oxygen vacancy in the system. Better thermal stability was observed for the samples with a small endothermic peak at 966 °C.

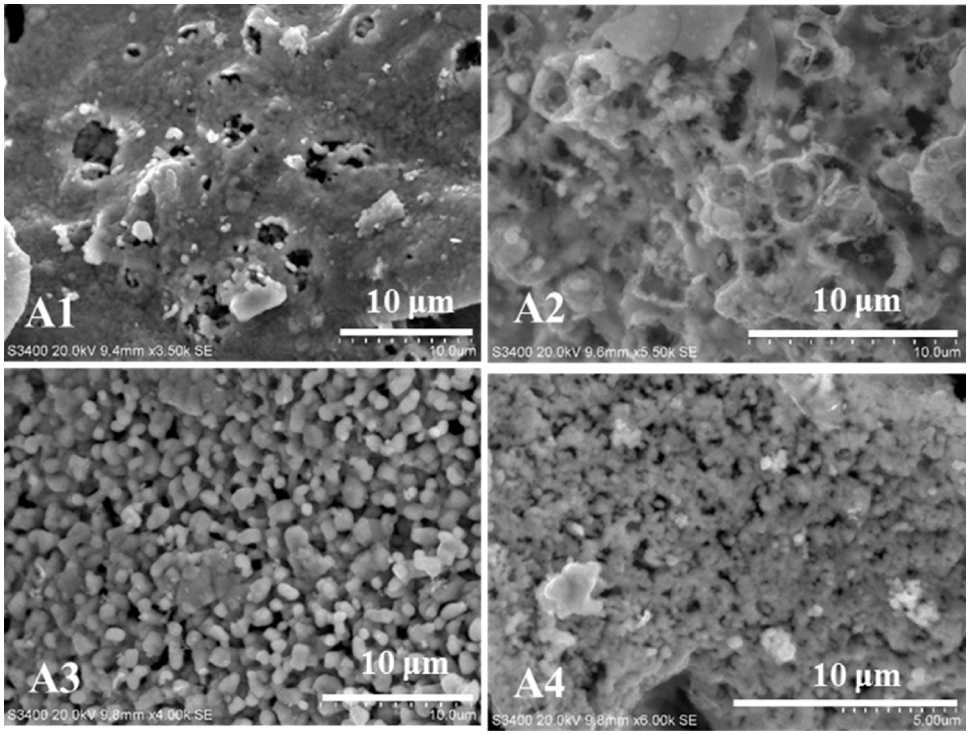

Fig. 2. SEM images of $Ag_{3(2+x)}In_xNb_{4-x}O_{11+\delta}$ ($0.25 \leq \times \leq 1.0$; A1–A4) nanoparticle.

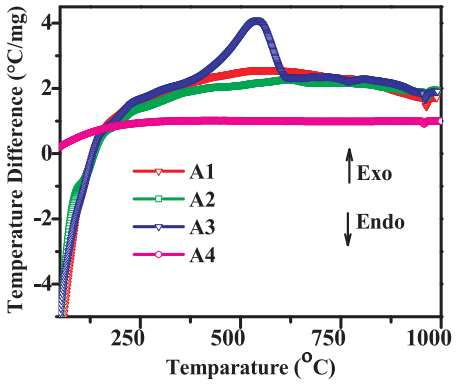

Fig. 3. DTA traces of $Ag_{3(2+x)}In_xNb_{4-x}O_{11+\delta}$ ($0.25 \leq \times \leq 1.0$; A1–A4) nanoparticle.

3.4. Diffuse reflectance spectroscopy (DRS) studies

Diffuse reflectance spectroscopy (DRS), has been employed to study the optical properties of the samples are shown in Fig. 4(a). The strong absorbance at 272 and 387 nm are due to inter-band charge transfer from O2- 2p electron states to Nb^{4+} 4d electron states [21]. Altering the composition, size and structure of the samples can be used to modify interband transitions and tailor the optical properties according to the desired application. Studies on interband electronic transitions are of practical importance for photonics, switchable plasmonics, photocatalysis and optoelectronics devices. In the present studied samples the interband transition inferred from DRS spectra indicates that the materials can act as light harvesting, energy conversion and photocatalytic materials. The energy band gaps were estimated using the Tauc plot method as shown in Fig. 4(b). The results show that the samples A1–A4 indicate an indirect band gap of 2.14, 2.13, 2.62 and 2.51 eV, respectively. The reported band gaps of other similar compounds such as $Na_2Ta_4O_{11}$, $PbTa_4O_{11}$, $Ag_2Ta_4O_{11}$, $Ag_2Nb_4O_{11}$ and $Ag_6Pr_1Nb_4O_{11}$ are 4.3, 3.95, 3.9, 3.30 and 3.40 eV respectively which are considered to be wide bandgap materials [22]. The present studied sample $Ag_{7.5}In_{0.5}Nb_{3.5}O_{11+\delta}$ also show a decrease of 1.17 eV when compared to the band gap of $Ag_2Nb_4O_{11}$ and Nb_2O_5 (3.40 eV) [23,24]. The Ag incorporation into the Nb_2O_5 decreases the band gap from 3.4 to 2.3 eV. Further integration of the In into the Ag-Nb system further decreases the band gap by 0.2 eV, suggesting that the valence band maximum

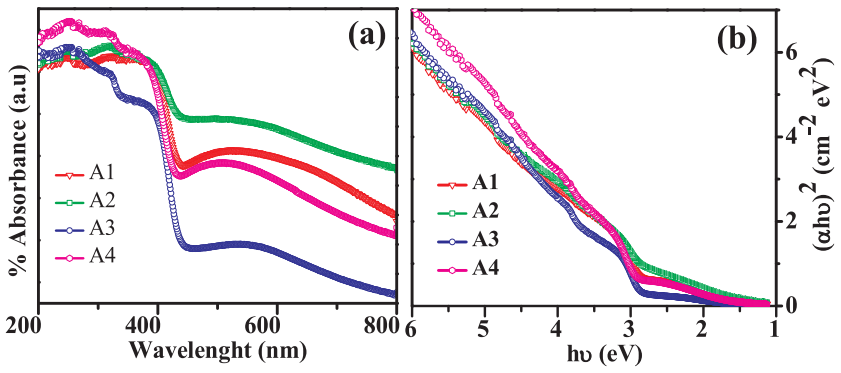

Fig. 4. (a) DRS spectra and **(b)** Tauc plot of $Ag_{3(2+x)}In_xNb_{4-x}O_{11+\delta}$ ($0.25 \leq \times \leq 1.0$; A1-A4) nanoparticle.

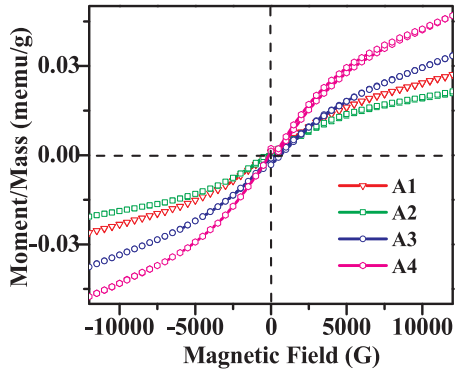

Fig. 5. Magnetization plot of $Ag_{3(2+x)}In_xNb_{4-x}O_{11+\delta}$ ($0.25 \leq \times \leq 1.0$; A1–A4) nanoparticles at 300 K.

(VBM) mostly involves of O2p orbitals, while the conduction band minimum (CBM) mostly involves of Nb-4d orbitals. Therefore, introducing Ag and In into the Nb_2O_5 crystal is expected to downshift the position of CBM and VBM remains at the same position [7]. The results reveal that the Ag and In ions have extended the range of absorbance of niobium oxides in the visible light. Hence, the sample can be used as photocatalyst under visible light and the narrow band gap is an advantage which can increase the photoresponse.

3.5. Magnetic studies

3.5.1. Vibrating sample magnetometer

Fig. 5 shows the magnetization (M–H) curve in the field range of ± 12,000 G at room temperature. The M–H curve appeared as sigmoid hysteresis shape with low remanence and coercivity, which indicates that the samples show a weak ferromagnetic behavior at 300 K. Magnetic susceptibility, (χ) of the samples are calculated using the relation (3) bellow,

$$M = \chi H \quad (3)$$

where M -Magnetization (emu/g) and H -Applied magnetic field. The calculated magnetic susceptibilities (χ) are in the order of 10^{-5} emu/gG which confirms the weak ferromagnetism of the samples. The magnetic parameters (χ, H_{ci} M_r and M_s) of the samples are given in Table 1. The nature of the hysteresis curve can help to understand the domain states of the magnetism. The hysteresis curve of the single domains is broader than a multi-domain state. This is because of the high coercivity (H_{ci}) and reminanent magnetization (M_r) of single domain state material. The low value of the H_{ci} and M_r of samples are shows the existence of nanocrystallites, which characterize the samples are soft magnetic materials. Since Ag^+ and In^{3+} are diamagnetic, the magnetic features are due to the presence of Nb ions. The reason for magnetism is mainly due to the double exchange interaction amongst polarized spin and conduction electrons of Nb ions. In addition, the presence of oxygen vacancies may form F centers with trapped electrons which overlap with metal d orbital (Nb-O_v-Nb) leads to ferromagnetic nature [25–28]. Thus, the ferromagnetism originates from the combination of double exchange interaction between the Nb ions and the presence of oxygen vacancy. The exchange interaction of the ions is too short which results weak ferromagnetism. The smooth hysteresis loop reveals the low residual strain, which exhibits good mechanical properties and homogeneity of the nanoparticle.

3.5.2. Electron spin resonance

To further understand the magnetic ordering by considering the presence of paramagnetic ions (Nb^{4+}) and the oxygen vacancy (O_V) we studied ESR response at 77 and 300 K (Fig. 6). The spin Hamiltonian parameters g values of the samples are presented in Table 1. The nuclear spin value of Nb^{4+} ion is 9/2; therefore, it should produce the hyperfine structure of ten lines. The sample A1 at 77 K show a poorly resolved hyperfine lineshapes with g_{iso} 2.039 and the other samples show only an isotropic peaks at g_{iso} 2.00, which are aggregates of reduced Nb^{4+} ions [29]. The decrease of the ESR lineshapes is due to several reasons, like spin-spin exchange interaction between the neighboring magnetic ions and a process linking redox phenomena [30]. The absence of hyperfine ESR lineshapes in the current study might be the relaxation process between Nb^{4+} ions. The reduced Nb^{4+} and O_V in the samples may lower the donor energy levels below the conduction band, this results increase the electron concentration. The O_V may also contribute to charge transfer and inhibit the charge recombination. These aspects can suggest that the samples can be used as photocatalysis which is in agreement with DRS results [31].

4. Conclusions

Multifunctional $Ag_{3(2+x)}In_xNb_{4-x}O_{11+\delta}$ ($0.25 \leq \times \leq 1.0$) nanoparticles with monoclinic lattice structure were successfully prepared by sol-gel technique. Purity and homogeneity of samples were confirmed by SEM- X-ray mapping. Optical and ESR studies have established the presence of reduced Nb^{4+} and O_V in the samples, which enhances greater light absorption in the UV–vis region. The magnetization studies show that the samples are weak ferromagnetic at 300 K. One of the major application, the developed material can offer is in the field of photocatalytic degradation of organic polluants, where narrow band photocatalysts under visible light activity is highly desired. Since the compounds are sensitive to magnetic field, these materials as magnetically seperable photocatalysts can also be explored in future.

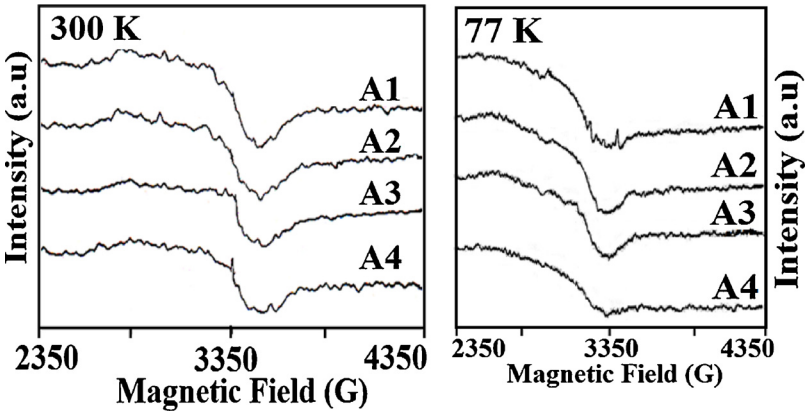

Fig. 6. EPR spectra of $Ag_{3(2+x)}In_xNb_{4-x}O_{11+\delta}$ ($0.25 \leq \times \leq 1.0$; A1–A4) nanoparticles at 300 K.

Acknowledgements

The author SR is thankful to Dr. Subhadra Ramesh, AJIMS Mangalore, India for her constant encouragement and Department of Materials Science, University of Chile, Chile, FONDECYT- Project N° 3170052 for financial support .

References

[1] C. Chen, H. Ning, S. Lepadatu, M. Cain, H. Yan, M.J. Reece, J. Mater. Chem. C 3 (2015) 19–22.
[2] D. Montasserasadi, M.W. Granier, L. Spinu, S.C. Rai, W. Zhou, J.B. Wiley, Dalton Trans. 44 (2015) 10654–10660.
[3] H. Wang, Z. Liang, Q. Liu, D. Zhang, J. Wang, Inorg. Chem. Commun. 61 (2015) 157–159.
[4] A. Niewiadomski, A. Kania, G.E. Kugel, M. Hafid, D. Sitko, Mater. Res. Bull. 65 (2015) 123–131.
[5] S. Ramesh, J.V. Ramaclus, E. Mosquera, B.B. Das, RSC Adv. 6 (2016) 6336–6341.
[6] M.E. Strayer, A.S. Gupta, H. Akamatsu, S. Lei, N.A. Benedek, V. Gopalan, T.E. Mallouk, Adv. Funct. Mater. 26 (2016) 1930–1937.
[7] N. Maso, D.I. Woodward, P.A. Thomas, A. Varez, A.R. West, J. Mater. Chem. 21 (2011) 2715–2722.
[8] N. Maso, A.R. West, J. Mater. Chem. 20 (2010) 2082–2084.
[9] R. Shao, X. Zeng, Z. Cao, H. Dong, L. Wang, F. Wang, J. Liu, Z. Li, Q. Liang, RSC Adv. 5 (2015) 102101–102107.
[10] E.S. Babu, S.K. Hong, Superlattices Microstruct. 82 (2015) 349–356.
[11] T. Feng, A.K. Ghosh, Indium oxide/n-silicon heterojunction solar cells, None, 1982, p. Medium: ED.
[12] A. Tubtimtae, M.-W. Lee, Superlattices Microstruct. 52 (2012) 987–996.
[13] J. Xu, J. Gao, Y. Liu, Q. Li, L. Wang, Mater. Res. Bull. 91 (2017) 1–8.
[14] D.-H. Kim, H.-K. Lee, J.-Y. Na, S.-K. Kim, Y.-Z. Yoo, T.-Y. Seong, Superlattices Microstruct. 83 (2015) 635–641.
[15] S.K. Kannan, P. Thirnavukkarasu, R. Jayaprakash, J. Chandrasekaran, V. Mohanraj, Mater. Sci. Semicond. Process. 50 (2016) 31–35.
[16] A. Kim, Y. Won, K. Woo, S. Jeong, J. Moon, Adv. Funct. Mater. 24 (2014) 2462–2471.
[17] S. Yan, H. Ou, L. Zhang, J. He, J. Yu, Mater. Res. Bull. 61 (2015) 120–123.
[18] A.M. Adam, E. Lilov, P. Petkov, Superlattices Microstruct. 101 (2017) 609–624.
[19] S. Ramesh, J. Nanosci. 2013 (2013) 1–8.
[20] J.H. Joshi, D.K. Kanchan, M.J. Joshi, H.O. Jethva, K.D. Parikh, Mater. Res. Bull. 93 (2017) 63–73.
[21] W. Wu, S. Liang, Z. Ding, H. Zheng, L. Wu, Solid State Sci. 13 (2011) 2019–2023.
[22] J. Boltersdorf, T. Wong, P.A. Maggard, ACS Catal. 3 (2013) 2943–2953.
[23] H. Dong, G. Chen, J. Sun, Y. Feng, C. Li, C. Lv, Chem. Commun. 50 (2014) 6596–6599.
[24] J.K. Dash, L. Chen, M.R. Topka, P.H. Dinolfo, L.H. Zhang, K. Kisslinger, T.M. Lu, G.C. Wang, RSC Adv. 5 (2015) 36129–36139.
[25] D.Y. Guo, Z.P. Wu, Y.H. An, X.C. Guo, X.L. Chu, C.L. Sun, L.H. Li, P.G. Li, W.H. Tang, Appl. Phys. Lett. 105 (2014) 023507.
[26] S. Ghosh, G.G. Khan, K. Mandal, ACS Appl. Mater. Interfaces 4 (2012) 2048–2056.
[27] A. Sundaresan, R. Bhargavi, N. Rangarajan, U. Siddesh, C.N.R. Rao, Phys. Rev. B 74 (2006) 161306.
[28] Y. An, S. Wang, D. Feng, Z. Wu, J. Liu, Appl. Surf. Sci. 276 (2013) 535–538.
[29] F. Dolci, M.D. Chio, M. Baricco, E. Giamello, J. Mater. Sci. 42 (2007) 7180–7185.
[30] R. Harani, C.A. Hogarth, K.A.K. Lott, J. Mater. Sci. 19 (1984) 1420–1427.
[31] W. Zhao, W. Zhao, G. Zhu, T. Lin, F. Xu, F. Huang, Dalton Trans. 45 (2016) 3888–3894.